Near Homogeneous Microphysics of the Record−Breaking 2020 Summer Monsoon Rainfall during the Northward Migration over East China

Long WEN, Wei ZHANG, Cha YANG, Gang CHEN, Yajun HU, Hao ZHANG

Related articles that may interest you

Seasonal Variations of Observed Raindrop Size Distribution in East China

Advances in Atmospheric Sciences. 2019, 36(4), 346   https://doi.org/10.1007/s00376−018−8107−5

Recent Progress in Dual−Polarization Radar Research and Applications in China

Advances in Atmospheric Sciences. 2019, 36(9), 961   https://doi.org/10.1007/s00376−019−9057−2

Diurnal Variation in the Vertical Profile of the Raindrop Size Distribution for Stratiform Rain as Inferred from Micro Rain Radar Observations in Sumatra

Advances in Atmospheric Sciences. 2020, 37(8), 832   https://doi.org/10.1007/s00376−020−9176−9

Statistical Characteristics of Raindrop Size Distribution in the Tibetan Plateau and Southern China

Advances in Atmospheric Sciences. 2017, 34(6), 727   https://doi.org/10.1007/s00376−016−5235−7

Moisture Origins and Transport Processes for the 2020 Yangtze River Valley Record−Breaking Mei−yu Rainfall

Advances in Atmospheric Sciences. 2021, 38(12), 2125   https://doi.org/10.1007/s00376−021−1097−8

The Record−breaking Mei−yu in 2020 and Associated Atmospheric Circulation and Tropical SST Anomalies

Advances in Atmospheric Sciences. 2021, 38(12), 1980   https://doi.org/10.1007/s00376−021−0361−2

AAS Website   AAS Weibo   AAS WeChat

Follow AAS public account for more information

• Original Paper •

Near Homogeneous Microphysics of the Record-Breaking 2020 Summer Monsoon Rainfall during the Northward Migration over East China

Long WEN[*1], Wei ZHANG[2], Cha YANG[1], Gang CHEN[*3], Yajun HU[2,4], and Hao ZHANG[1]

[1]*Xichang Satellite Launch Center*, *Xichang* 615000, *China*

[2]*Xiamen Key Laboratory of Strait Meteorology*, *Xiamen* 361012, *China*

[3]*Key Laboratory of Transportation Meteorology of China Meteorological Administration*, *Nanjing Joint Institute for Atmospheric Sciences*, *Nanjing* 210041, *China*

[4]*Xiangan Meteorological Bureau*, *Xiamen* 361103, *China*

ABSTRACT

Knowledge of the raindrop size distribution (DSD) is crucial for disaster prevention and mitigation. The record-breaking rainfall in the summer of 2020 caused some of the worst flooding ever experienced in China. This study uses 96 Parsivel disdrometers and eight-year Global Precipitation Measurement (GPM) satellite observations to reveal the microphysical aspects of the disastrous rainfall during its northward migration over East China. The results show that the nearly twice as heavy rainfall in Jiangsu Province compared to Fujian Province can be attributed to the earlier-than-average northward jump of the summer monsoon rainband to the Yangtze-Huaihe River valley. The persistent heavy monsoon rainfall showed similar near-maritime DSD characteristics, with a higher concentration of small raindrops than the surrounding climatic regimes. During the northward movement of the rainband, the DSD variables and composite spectra between the pre-summer rainfall in Fujian and mei-yu rainfall in Jiangsu exhibited inherent similarities with slight regional variations. These are associated with similar statistical vertical precipitation structures for both convective and stratiform rain in these regions/periods. The vertical profiles of radar reflectivity and DSD parameters are typical of monsoonal rainfall features, implying the competition between coalescence, breakup, and accretion of vital warm rain processes. This study attributes the anomalously long duration of the mei-yu season for the record-breaking rainfall and reveals inherent homogeneous rainfall microphysics during the northward movement of the summer monsoon rainband. The conclusion is statistically robust and would be helpful for accurate precipitation estimation and model parameterization of summer monsoon rainfall over East China.

Key words: precipitation microphysics, raindrop size distribution, mei-yu, East China

Article Highlights:

- The record-breaking summer rainfall in 2020 was mainly attributed to an extended duration of heavy rainfall with near-maritime raindrop size distributions.
- The vertical structure and microphysics of summer rainfall remained nearly homogeneous during the northward migration of the East Asian summer monsoon.
- Vital warm rain processes during moderate convective rainfall have resulted in near-homogeneous rainfall microphysics over East China.

---

1. Introduction

Knowledge of the raindrop size distribution (DSD) characteristics and variability is crucial to better understand precip-

itation microphysics. The DSD variations and their derivatives (e.g., the derived and retrieved integral parameters, relationships, and constructed scattering models) over different regions have been extensively investigated in recent years (Rosenfeld and Ulbrich, 2003; Wen et al., 2016; Zhang et al., 2019b; Murali Krishna et al., 2021; Raut et al., 2021; Ryu et al., 2021; Lai et al., 2022; Wang et al., 2022). In addi-

---

* Corresponding authors: Long WEN, Gang CHEN

Emails: wenlong@smail.nju.edu.cn, chengang@cma.gov.cn

tion to many application fields, this vital information is essential for estimating precipitation accurately and establishing precise model microphysics parameterizations (Zhang et al., 2001).

Summer (May–September) is the rainy season in East China when rainfall accounts for more than 40% of the annual total (Li and Mao, 2019). Typically, with the onset of the East Asian summer monsoon (EASM), a quasi-stationary subtropical mei-yu front (Tao and Chen, 1987), associated with a major monsoon rainband, was established from the Bay of Bengal to the South China Sea in early May. It then advances to the continent with the northward march of the EASM, bringing pre-summer rainfall to South/East China (including Taiwan) from late May to early June. Subsequently, the rainband remains around the Yangtze-Huaihe river valley (YHRV) from mid-June to mid-July (the commonly known mei-yu season), followed by a rapid jump over North China and Korea in late July (Ding and Chan, 2005).

In 2020, the duration of the mei-yu season in the YHRV was 62 days, during which time rainfall amounts reached ~759.2 mm (twice the average). Both the mei-yu duration and associated rainfall amounts have broken the historical record and caused the worst flooding in the YHRV since 1961 (Ding et al., 2021; Zhou et al., 2021). The floods killed at least 200 people, flattened approximately 30,000 houses, and caused economic losses of over 170 billion yuan (Zhou et al., 2021). The causal synoptic features, subseasonal variability, and extreme events have been extensively investigated (Clark et al., 2021; Ding et al., 2021; Niu et al., 2021; Qiao et al., 2021). Significant contributing factors to the long-lasting (early onset and late withdrawal) and extreme mei-yu rainfall are belived to include the record strength of the Indian Ocean dipole event in 2019 (Takaya et al., 2020; Zhou et al., 2021), the sub-seasonal phase transition of the North Atlantic Oscillation (Liu et al., 2020), the exceptionally persistent Madden-Julian Oscillation activity (Zhang et al., 2021), and Tibetan Plateau vortices (Li et al., 2021).

Over the last few years, with the advancement of precipitation microphysics measurement techniques, summer/mei-yu rainfall studies have been extensively investigated and have reported various DSD characteristics over East Asia. For example, three-year Parsivel observations during mei-yu in Nanjing, East China (Chen et al., 2013) showed a slightly lower concentration but larger raindrop size than mei-yu/baiu in Japan (Bringi et al., 2006). Jin et al. (2015) found that convective rain in Chuzhou, Anhui Province contains a higher concentration of smaller raindrops than in Nanjing (~90 km west). Since then, both disdrometer and polarimetric radar observations in Nanjing (Wen et al., 2016, 2020) demonstrated a higher concentration of smaller raindrops compared to Chen et al. (2013) and Bringi et al. (2006). For comparison, monsoonal stratiform precipitation over South China exhibits larger diameters (Huo et al., 2019) and a higher concentration of small-sized drops (Tang et al.,

2014) than the observed droplet spectrum in East China. In South and East China, convective rainfall shows significant regional differences, with similar average raindrop diameters, but at lower concentrations than in maritime clusters (Tang et al., 2014). Recently, DSD parameters in Fujian Province showed features consistent with those in South China, with higher droplet concentrations and smaller diameters than in East China (Hu et al., 2022b). Many small-sized raindrops in Taiwan with some geographic-dependent variations have also been reported (Seela et al., 2017).

In summary, among the various regional differences, a higher concentration of small-sized raindrops in East China compared to other climate regimes covered by the EASM rainband could be roughly elicited from the literature. Those previous results imply a "maritime" or "maritime-like" nature of convective DSD over East China (Chen et al., 2013; Tang et al., 2014; Jin et al., 2015; Wen et al., 2016, 2017b; Zhang et al., 2019a). It is recognized that DSDs vary across different rain types, rainfall systems, climate regimes, and topographies (Rosenfeld and Ulbrich, 2003; Wen et al., 2019). However, these studies have been limited to observations from only one or a few stations and thus place more emphasis on their differences rather than similarities. The insufficient data samples, lack of spatial representativeness, and different sampling times in each study may all lead to variability and uncertainty in the analyses. These potentially led to the different and unstable results of DSD characteristics obtained in each study, which impedes the attainment of a general and robust conclusion for EASM rainfall microphysics over contiguous China. To achieve a precise and generally applicable microphysical parameterization for modeling efforts in this specific region, efforts are needed to summarize some commonalities in the diversity of EASM rainfall microphysics in a statistical sense.

Moreover, the microphysics of the record-breaking summer rainfall in 2020 has not yet been investigated. It is not entirely known whether the characteristics that made the 2020 summer/mei-yu rainfall a record-breaking event over East China differed from the climatological EASM DSD. We previously revealed that the DSD characteristics of each rain type (convective, stratiform, and shallow) remained essentially unchanged throughout summer in East China (Wen et al., 2016). Under the control of a similar large-scale circulation in the EASM season, what were the DSD variations during the northward movement of this annual quasi-stationary mei-yu front and the interrelated monsoon rainband? Addressing these issues would aid in better understanding monsoon rainfall microphysics and potentially lead to more accurate parameterizations and predictions of EASM rainfall. Here, with the use of a dense array of OTT Particle Size and Velocity disdrometer (Parsivel) network observations, the subjects of this study were 1) to reveal the microphysics of the historic 2020 summer rainfall and 2) to further examine whether the precipitation microphysics varies or shows commonality along with the northward migration of the EASM rainband, typically from the pre-summer season

to the mei-yu season over East China.

The remainder of this paper is organized as follows. Section 2 describes the data and methodology, section 3 presents the results, and section 4 provides a conclusion and discussion.

2.   Data and Methods

2.1.   *DSD dataset*

The DSD datasets used in this study were collected from 30 Parsivel disdrometer measurements of pre-summer season rainfall in Fujian (FJ) Province and 66 mei-yu season rainfall measurements in Jiangsu (JS) Province (Fig. 1). The second-generation Parsivel disdrometer (Tokay et al., 2014) was equipped with a laser sheet (180 mm long and 30 mm wide). It measures (estimates) the size and fall velocity of the particles from the maximum attenuation and duration of the particles falling through the laser sheet. Considering the edge effect of the sampling, the effective sampling area was $180 \times (30 - D/2)$, where D is the raindrop diameter (Tokay et al., 2013). The procedure then binned the signals into a 32×32 matrix with size and velocity ranging from 0 to 25 mm and 0 to 22.4 m s^{-1}, respectively. The first two size classes were left empty because of their low signal-to-noise ratio, and the smallest detectable size was 0.312 mm in diameter.

Some a priori assumptions were made during the observation, data processing, and analysis of the Parsivel measurements. For example, the "spheroidal" assumption does not account for the shape of the drop, and the "one drop at once" assumption assumes that only one particle is in the beam at any one time (see details in Wen et al., 2017b). Moreover, when the 1D laser signal measures one or a few small-sized drops, they may be blocked by a large one while passing through the sensor area, or the shadow of two or more drops overlaps and is incorrectly recognized as a larger one. These assumptions and working principles are inconsistent with natural rainfall, which could potentially result in the underestimation of small drop concentrations and the overestimation of large drop diameters (Tokay et al., 2013; Wen et al., 2017b). Therefore, a size-correction procedure was recommended (Battaglia et al., 2010). Despite the above-mentioned shortcomings, Parsivel is the most widely used tool and has demonstrated exemplary performance in capturing primary DSD characteristics (Tokay et al., 2014). The easy-to-operate features and capability to identify various precipitation types have made the Parsivel a present weather sensor to replace manual observations at over 2300 county-level meteorological stations by the China Meteorological Administration (CMA) in 2019.

The temporal resolution of DSD data was 1 min. Raindrops larger than 8 mm were eliminated because of the significant uncertainties and rare occurrences in natural rain. For each 1-min sample, if the total number of drops is less than 10 or the derived rain rate is less than 0.1 mm h^{-1}, the sample was disregarded as a bias/noise. Therefore a fall-velocity-based filter was applied to eliminate oversampling errors and spurious raindrops resulting from wind-caused turbulence, splash contamination, and other biases (Wen et al., 2019). As officially determined by the CMA, the pre-summer
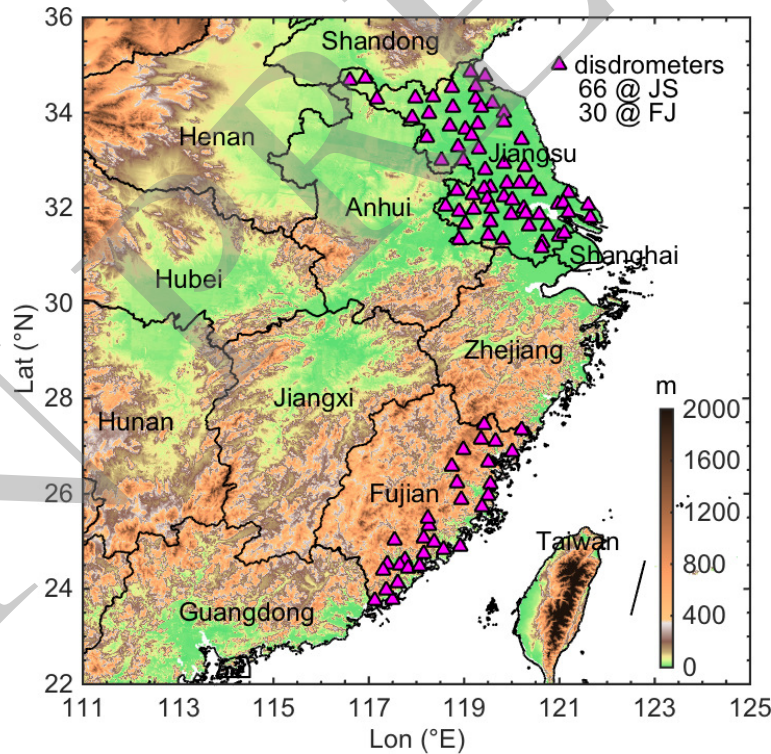
Fig. 1. The topography (shading, m) and location of Parsivel disdrometer stations (magenta triangle) in Fujian and Jiangsu provinces.

season in FJ is between 18 May and 27 June, and the mei-yu season in JS is from 9 June to 20 July 2020. A total of 153 463 min of pre-summer season DSD samples from FJ and 555 079 mei-yu samples from JS were obtained after quality control.

A widely used method to distinguish between convective and stratiform rain types is based on continuous rainfall intensity and its standard deviation (Bringi et al., 2003). However, Bringi's scheme usually excludes considerable data samples as either an uncategorized or mixed type. For example, ~ 29.2% and 21.1% of the data samples were excluded by Chen et al. (2013) and Wen et al. (2016), respectively. More importantly, the Bringi scheme would have excluded ~ 57.73% and 57.66% of the total rainfall amount as uncategorized samples for the FJ and JS datasets, respectively. Therefore, for simplicity and to retain as many data samples as possible, a rain rate R of 10 mm h^{-1} was used to separate the convective ($R>10$ mm h^{-1}) and stratiform ($R<10$ mm h^{-1}) rain in this study, which has also been widely applied in the literature (Tokay and Short, 1996; Uijlenhoet et al., 2003; Thurai et al., 2010; Lane et al., 2018; Wen et al., 2018; Chang et al., 2019; Ryu et al., 2021; Zheng et al., 2021). The simple $R = 10$ mm h^{-1} threshold is reasonable for separating stratiform from convective rain types (Uijlenhoet et al., 2003; Thurai et al., 2010). This procedure produced 7577 and 14 5886 min of convective and stratiform samples in FJ, and 37 655 and 517 424 min in JS, respectively.

After the 1-min DSD samples were obtained, the bulk integral rainfall and DSD parameters were derived from the n-th order weighted moment of the measured DSD and fall velocity. The parameters discussed in this study included the total count of raindrops C_t, the total concentration of raindrops N_t (m^{-3}), liquid water content LWC (g m^{-3}), rain rate R (mm h^{-1}), radar reflectivity factor Z (mm^6 m^{-3}), mass-weighted mean diameter D_m (mm), and generalized intercept parameter N_w (mm^{-1} m^{-3}). These parameters were directly calculated from the measured DSDs without any assumption of the DSD form. Moreover, the gamma-DSD model's shape parameter μ and slope parameter Λ (mm^{-1}) were computed using the truncated moment fitting method (TMF, Vivekanandan et al., 2004) with the second, fourth, and sixth moments (M246) of the DSDs. The M246 method was applied in our previous studies (Wen et al., 2017a, 2020) to accurately retrieve the DSD parameters from polarimetric radar observations. More detailed expressions of the above parameters were given by Wen et al. (2016).

2.2. *Monthly rainfall, ERA-5, and GPM dataset*

The 1-km monthly precipitation dataset for China (Peng, 2020) and the hourly 0.25° × 0.25° output of the fifth-generation global atmospheric reanalysis from the European Center for Medium-Range Weather Forecasts (ERA-5, Hersbach et al., 2020) were applied to illustrate the distribution of monthly rainfall at the surface and the synoptic environment background.

Moreover, eight years (2014–21) of the Global Precipitation Measurement Satellite Dual-Frequency Precipitation

Radar level-2 dataset (GPM-2ADPR, version 7, (Seto et al., 2021)) were used to examine the vertical structure of precipitation microphysics in the two study areas of FJ (115°– 122°E, 22°–29°N) and JS (116°–122°E, 30.5°–35.5°N). The DPR operating at the Ku and Ka bands provides three-dimensional rainfall and DSD retrievals at a 5-km spatial and 125-m vertical resolution (Iguchi et al., 2021). Recent studies have validated the accuracy and potential applicability of GPM-DSD retrievals in China (Sun et al., 2020; Huang et al., 2021; Chen et al., 2022; Hu et al., 2022a). The official products applied here are the attenuation-corrected radar reflectivity factor Z_e at the Ku band, and the retrieved D_m and N_w values in the inner swath of the scan. The official DPR precipitation type products (convective and stratiform) were also applied, and the shallow rain (categorized as convective precipitation in the GPM) was excluded.

3. Results

3.1. *The record-breaking rainfall in the summer of 2020*

According to the literature, the extremely warm SST in the tropical Indian Ocean (Wang et al., 2021a) induced a westwardly extended anticyclone of unprecedented strength in the subtropical western Pacific (Clark et al., 2021) relative to climatology. The vital water vapor transport by the anomalous anticyclone, associated with the anomalous ascending motions induced by the enhanced southwesterly jet, caused heavy and persistent rainfall over East China during the summer of 2020 (Niu et al., 2021; Wang et al., 2021b).

Figure 2 shows the environmental background in May, June, and July from the ERA-5 reanalysis. The location of the summer monsoon rainband is primarily determined by the western Pacific subtropical high (WPSH, Ding and Chan, 2005). Specifically, after the onset of the EASM in May 2020, a monsoonal rainband was positioned over South/Southeast China to South Japan (Figs. 2a–c). The resulting rainfall center was located over Guangdong, north FJ, and Taiwan (Fig. 2d). The WPSH then jumps northward in early June (two weeks earlier than the climatology, Ding et al., 2021). Its ridgeline lies north of 20°N after the jump (Fig. 2e). During this period, South China and FJ were controlled by the WPSH, and the relative humidity and vorticity in FJ were much lower; consequently, there were fewer rainy days than usual.

In contrast, the strengthened southwesterly flow carried abundant moisture from the ocean to the YHRV and converged with cold air from Northeast Asia (Figs. 2f, g, j, k). Subsequently, the slowly northward-moving rainband was subjected to increased convective instability and the early onset of the heaviest and most persistent mei-yu rainfall over the YHRV (Figs. 2h, l). Owing to the earlier northward migration, the rainfall in FJ and JS was approximately –50% and +50%~150% that of climatology, respectively (Niu et al., 2021; Zhou et al., 2021).

The disdrometer observed relative rainfall contributions from convective versus the total rainfall amount at each site
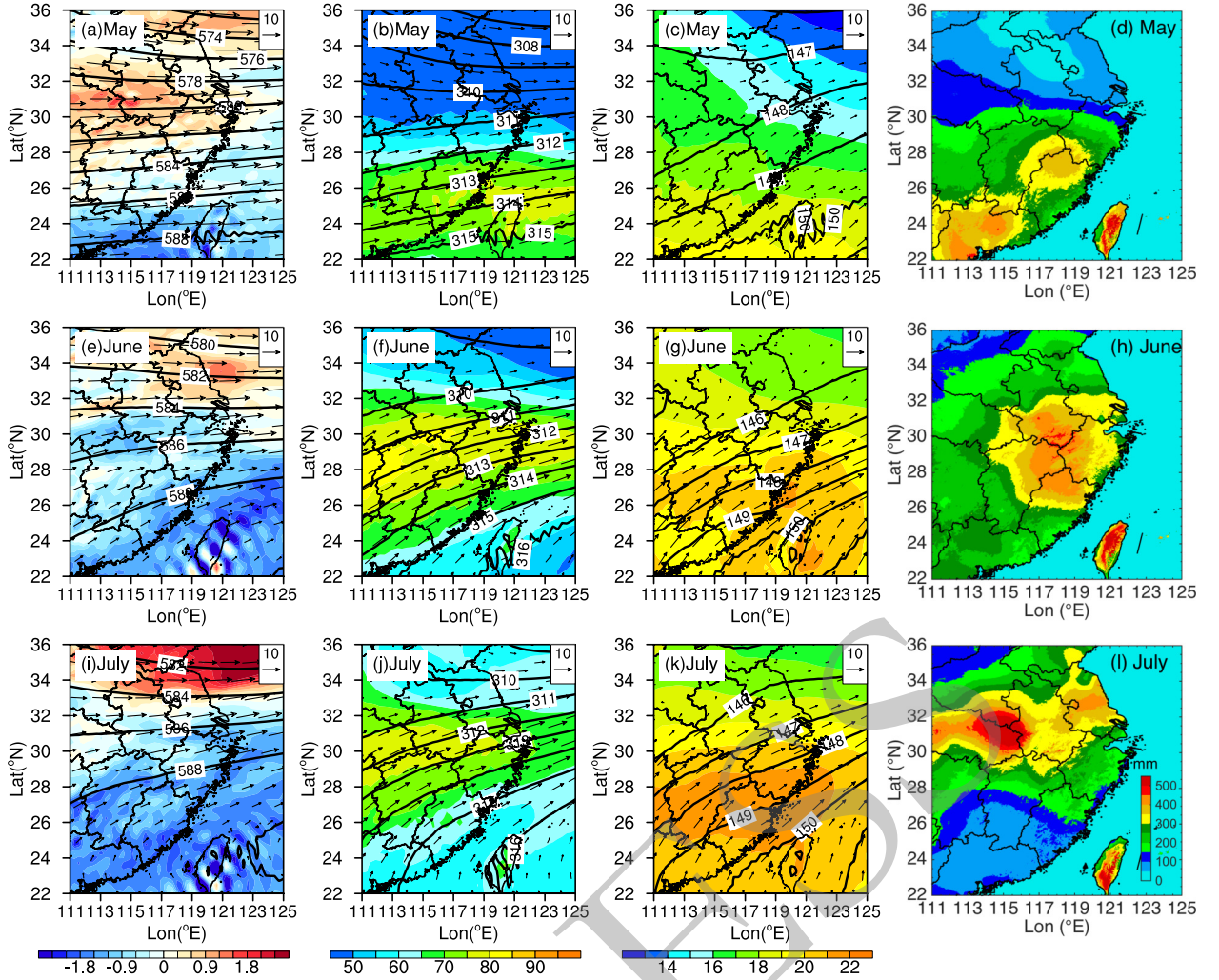
Fig. 2. Monthly mean horizontal wind (wind arrows, m s^{-1}), geopotential height (contour, hPa), and (a, e, i) 500-hPa absolute vorticity (shading, 10^{-5} s^{-1}), (b, f, j) 700-hPa relative humidity (shading, %), and (c, g, k) 850-hPa temperature (shading, °C) from the ERA-5 reanalysis in (top) May, (middle) June, and (bottom) July. The distribution of the monthly rainfall amount (mm) in (d) May, (h) June, and (l) July.

is shown in Fig. 3a. Considering the expected variations at each site, the Parsivel-observed convective rainfall contribution was comparable between JS (47.89%) and FJ (45.47%). The observed maximum rainfall amount during the mei-yu season in JS was 707.33 mm, whereas that during the pre-summer season in FJ was 312.36 mm. On average, stations in JS experienced rainfall that was nearly twice as heavy than in FJ, with respective depths of 439.64 mm and 225.65 mm. The mean convective daily rainfall amount for FJ and JS was 2.52 and 5.13 mm d^{-1}, with the daily number count of 1-min samples being 120.51% higher in JS (Fig. 3b). The respective daily amounts of stratiform rain were 2.89 and 5.34 mm d^{-1}, and there were 62.62% more samples in JS (Fig. 3c). Generally, the duration of pre-summer rainfall in FJ is significantly lower than usual, while the mei-yu rainfall in JS showed the opposite effect.

3.2. *The DSD characteristics*

The spatial distributions of the averaged D_m and N_t

from each site in FJ and JS are shown in Fig. 4. The vast majority of the averaged convective N_t for pre-summer rainfall in FJ was concentrated around 1000 to 1600 m^{-3}, with 3 out of 30 sites being between 800–1000 m^{-3}. The convective N_t of the mei-yu rainfall in JS was approximately 800–1200 m^{-3}, with 5/66 sites between 600–800 m^{-3}. Despite the regional variability, the pre-summer rainfall is generally characterized by a slightly higher N_t (~200 m^{-3}) than the mei-yu rainfall for both convective and stratiform rain, while the differences in D_m are negligible. In both FJ and JS, the distance between two random observational sites ranges from several kilometers to over 500 km. Considering the wide range of observations, the variability of D_m and N_t within (and between) the pre-summer and mei-yu seasons was small. The results from the dense network of DSD observations over such a wide range may imply near-homogeneous microphysical characteristics during the two periods in the two study areas.

The distribution of the averaged D_m–lgN_w pairs at each
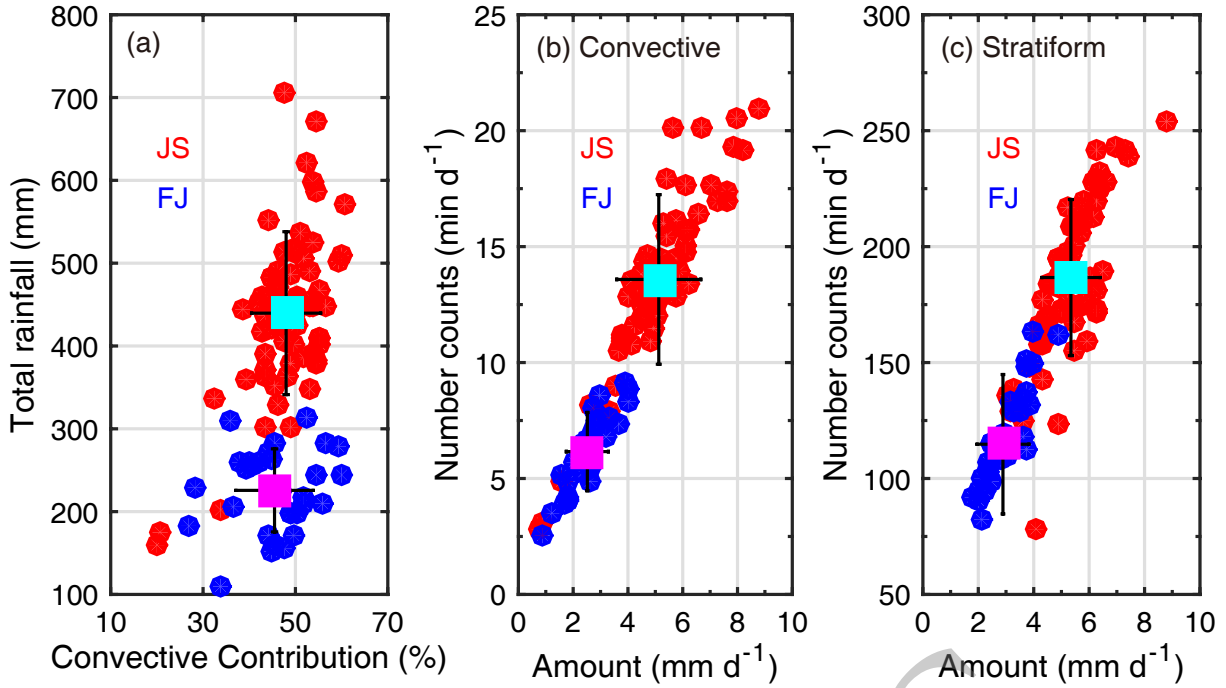
Fig. 3. (a) Rainfall contribution of convective versus total rainfall amount from disdrometer observations, and the rainfall amount versus number counts of raining minutes per day for (b) convective and (c) stratiform rain in FJ (blue dots) and JS (red dots). Error bars represent the standard deviation of the averaged values.

site also showed inherent similarities between the pre-summer and mei-yu rainfall (Fig. 5). The stratiform D_m–$\lg N_w$ pairs from FJ and JS showed substantial negative correlation coefficients (CC=–0.89 and –0.77), nearly overlapping with each other. The fitted D_m–$\lg N_w$ linear relationships using the least-squares method had similar slopes (–1.71 and –1.75), and the same intercept value (5.56), with the coefficient of determination (R^2) higher than 0.6 and the root mean square error (RMSE) lower than 0.09. As suggested by Bringi et al. (2003), the reverse distribution of the D_m–$\lg N_w$ line reflects the different microphysical processes of stratiform rain, ranging from the melting of tiny graupel or smaller rimed ice particles to the melting of large dry snowflakes. The fitted stratiform lines lie to the left of the "stratiform line" in Bringi et al. (2003) with similar negative slopes. This suggests that stratiform rain during the EASM in East China remained steady while moving northward from FJ to JS, with a smaller raindrop diameter than that of the other climatic regimes.

The convective D_m–$\lg N_w$ pairs were located around the lower right of the "maritime cluster" in Bringi et al. (2003), implying the near-maritime nature of convective rain in East China. Remarkably, straight convective D_m–$\lg N_w$ lines were also fitted, as the pairs exhibited a stronger correlation (CC= –0.93 and –0.91) than stratiform rain. The pre-summer line was located to the northeast of the mei-yu line because of the slightly higher concentration of raindrops in FJ. Meanwhile, R^2 was higher, whereas the RMSE was smaller for the fitted convective lines, suggesting a stronger negative correlation between D_m and $\lg N_w$ in convective rain for both FJ

and JS.

It is worth noting that although a different rain type classification method was applied in this study, the D_m–$\lg N_w$ distribution obtained here showed only minor differences compared to that when using the Bringi et al. (2003) scheme. Therefore, the comparative results were general and acceptable. Moreover, based on the distribution of D_m–$\lg N_w$ pairs using multisource observations from one or a few stations in the same/surrounding climatic regimes, previous DSD studies usually announce the finding of a different characteristic compared with the others. However, such findings are inconclusive because many factors contribute to these "differences". One of the main reasons for this is the lack of spatial representativeness, with insufficient data samples from one or a few stations.

Using observations from the dense disdrometer network, the features of the statistical EASM rainfall D_m–$\lg N_w$ pairs recognized here demonstrate that the "differences" in the literature are mainly within the deviations between each site. For example, for convective rain, the summer rainfall in Guangdong, South China (Huo et al., 2019, right triangle), mei-yu rainfall in Hubei, Central China (Fu et al., 2020, plus), and summer/mei-yu rainfall in Taiwan (Chen, 2009, diamond), and Jiangsu (Chen et al., 2013, pentagram; Wen et al., 2017b, down triangle), East China, are all plotted around the derived convective lines. Their averaged stratiform D_m–$\lg N_w$ pairs are less diverse and lie between the stratiform lines of Bringi et al. (2003) and the newly derived ones.

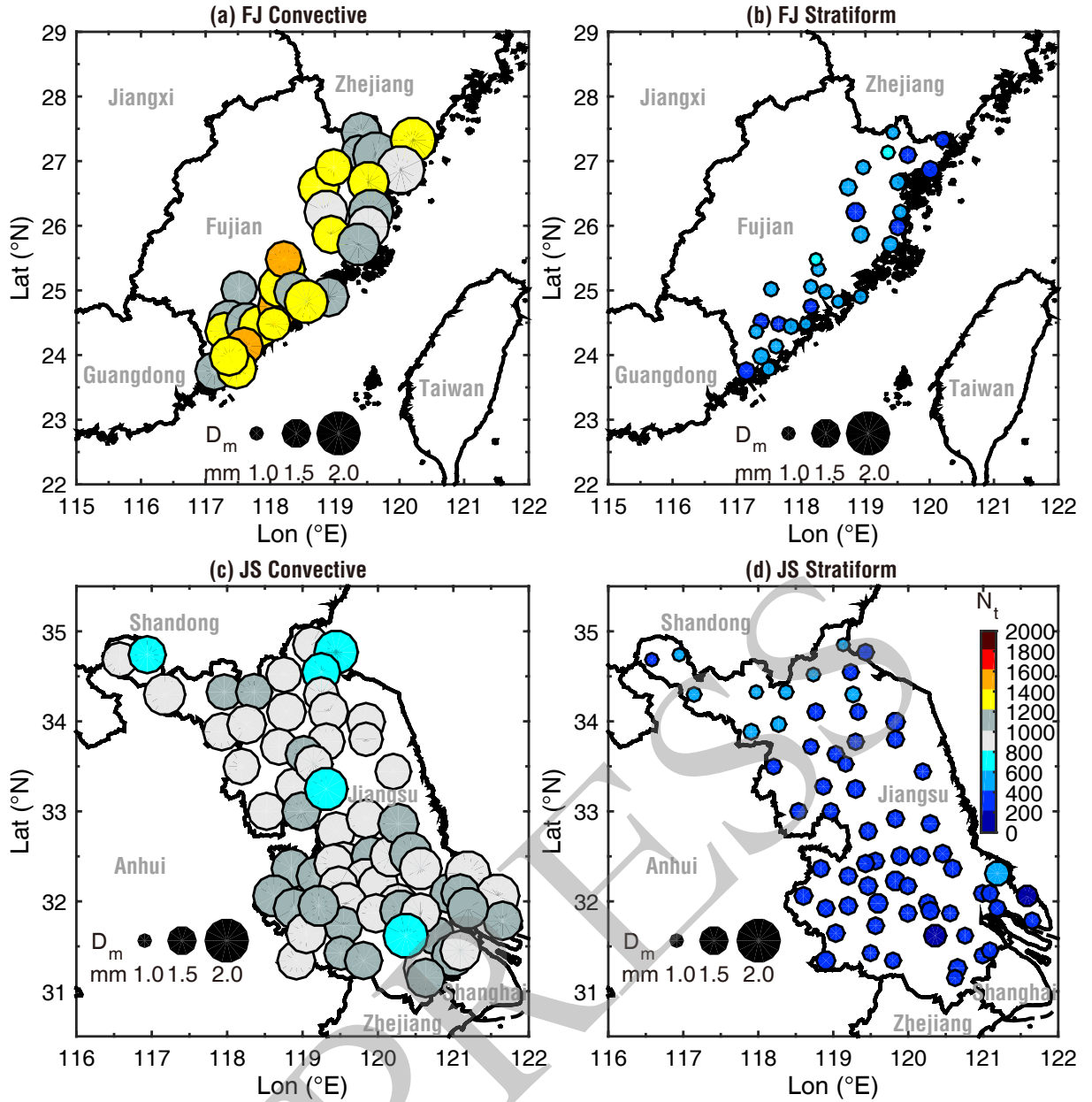The large dataset of 96 OTTs observations in this study

Fig. 4. Averaged convective and stratiform D_m (dot sizes) and N_t (colors) at each site in (a, b) FJ and (c, d) JS.

aids us in the effort of determining whether there is some commonality besides the spatial (FJ and JS) and temporal (presummer and mei-yu rainfall) diversity of EASM rainfall microphysics. In this case, the results implied that the "differences" obtained in previous studies should be largely recognized as a deviation in DSD at a specific site and can be well represented by the general characteristics of EASM rainfall microphysics. The similarity in the derived D_m–lgN_w lines can be considered a valid and reasonable indicator.

Generally, the overlap of averaged D_m–lgN_w pairs from 30 sites in FJ and 66 sites in JS (with similar coefficients of linear fitting), as well as the similarities with the results in the literature, suggest near-homogeneous microphysical characteristics during the northward migration of summer monsoon rainfall, typically from the pre-summer rainfall in

South/Southeast China to mei-yu rainfall in the YHRV.

The distributions and statistics of various DSD parameters for the pre-summer and mei-yu rainfall were further compared with the average value and standard deviation in each panel (Fig. 6). Both convective and stratiform rain showed similar distribution patterns for the bulk DSD parameters between the pre-summer and mei-yu rainfall. While most convective and stratiform D_m values range from 1 to 3 mm and 0.5 to 2 mm, respectively, and their distributions all have negative skewness. In contrast, the skewness of convective lgN_w (and lgN_t) is positive, with a much narrower range than its stratiform counterpart. This suggests large numbers of smaller raindrops in intense rainfall. Because of the slightly higher concentration of raindrops, the corresponding convective Z, R, and LWC values during pre-summer rainfall
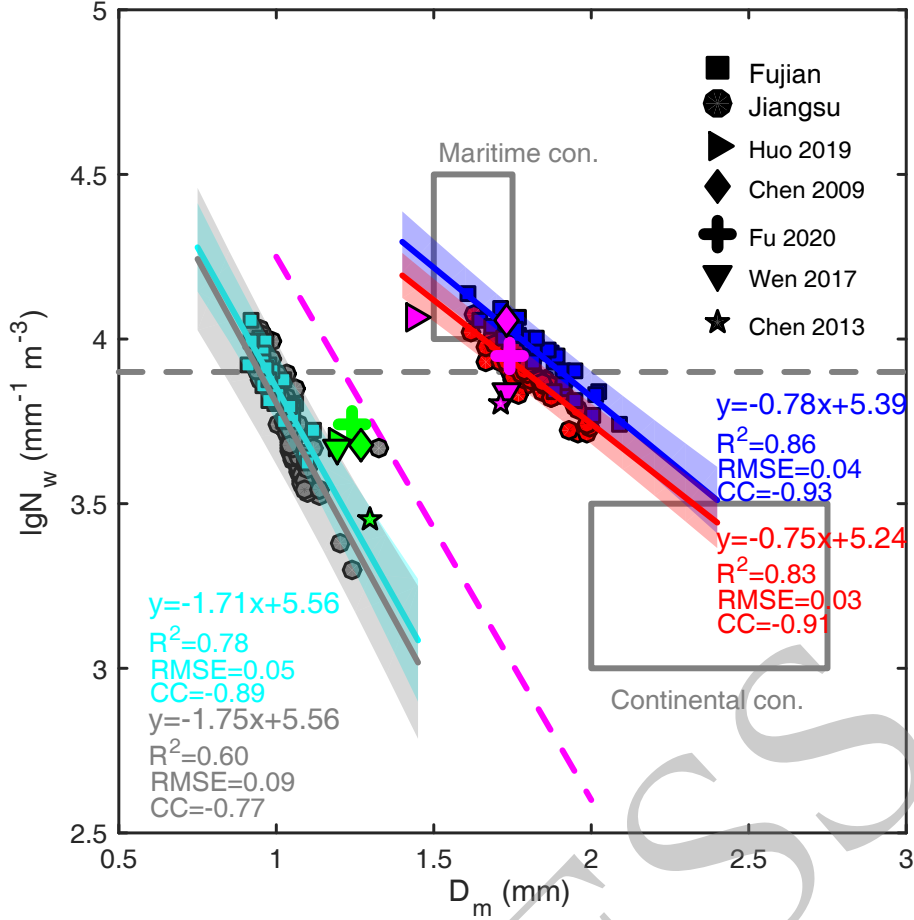
Fig. 5. Scatterplot of averaged D_m–lgN_w pairs from each site. The blue and cyan squares represent convective and stratiform rain in FJ, and the red- and black-filled circles represent convective and stratiform rain in JS, respectively. The gray rectangles and the pink dashed line correspond to the maritime and continental convective cluster and stratiform line in Bringi et al. (2003). The pink and green symbols represent the averaged convective and stratiform values from the literature. The fitted convective and stratiform lines and relations for convective and stratiform rain for FJ and JS are provided with the corresponding colors. The shading represents the 95% confidence interval of the fitting. CC = correlation coefficient; R^2 = coefficient of determination; RMSE = root mean square error.

were slightly larger than those during mei-yu rainfall. The distributions of μ and Λ also exhibited consistent characteristics between these two periods/areas. The only noticeable difference was the higher average C_t value for pre-summer rain in FJ. This phenomenon may have resulted from the higher environmental moisture content in FJ, which is much closer to the South China Sea (the primary water vapor source). Overall, the difference in the DSD parameters (except C_t) between the pre-summer and mei-yu rainfall was minor and smaller than the standard deviation within each period/area.

For comparison, the derived integral rain parameters for convective and stratiform rain during 2020, as well as those from Wen et al. (2017b) for the 2014–15 mei-yu rainfall in Nanjing, Jiangsu province, and Hu et al. (2022b) for the 2019 monsoon rainfall in Xiamen, Fujian province are presented in Table 1. For convective rain, the difference in D_m is within ±0.1 mm, while lgN_w (and N_t) have the highest values

in Hu et al. (2022b). The slightly higher raindrop concentrations (and the resulting higher R and LWC) in FJ than in JS from the literature are consistent with the present work. For stratiform rain, the differences are considerable but still within the standard deviation of each DSD parameter. These results imply that observations from one or a few stations are not necessarily statistically conclusive to address a "different" characteristic and that regional variability should be reasonably considered to reach a general conclusion.

For comparison, the composite spectra of different rain types, R classes, and Z classes also exhibited substantial similarities between the pre-summer and mei-yu rainfall (Fig. 7). All the spectra have peak concentrations mostly in the diameter range of ~0.5 mm with a sharp drop-off towards smaller sizes. It is a typical Parsivel-observed size spectrum at the small end (Tokay et al., 2013; Wen et al., 2016). The role of instrument limitations on missed small-sized drops, and
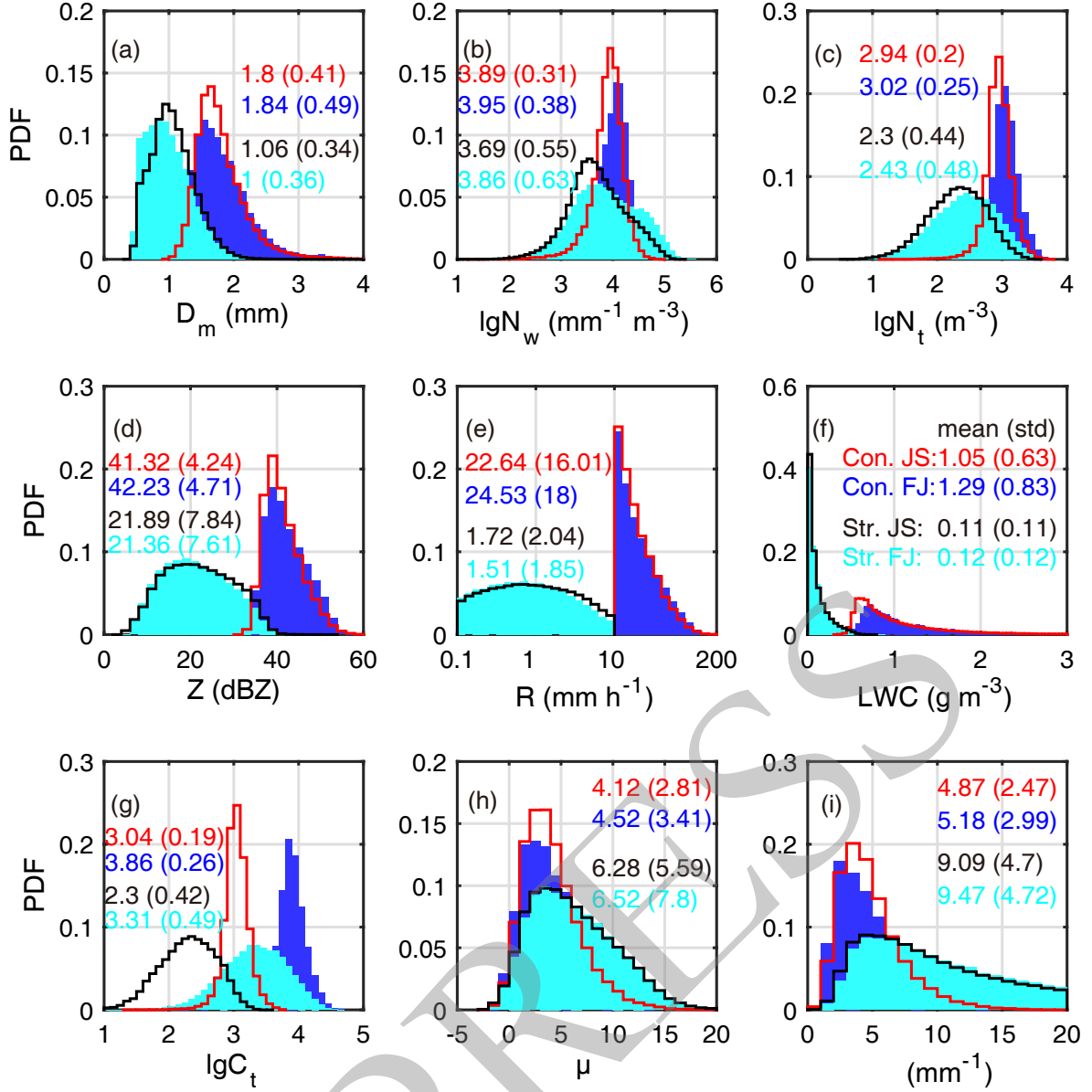
Fig. 6. Histograms of DSD variables and spectra for convective and stratiform rain in FJ and JS. (a–i) Red and black curves: convective and stratiform rain in JS; blue and cyan bars: convective and stratiform rain in FJ, respectively. The averaged value and its standard deviation are given in each panel with the corresponding color.

Table 1. Integral rain parameters as derived from the composite raindrop spectra of convective and stratiform rain in FJ and JS and previous studies in each region.

Rain type	Studies	Years	D_m	lgN_w	N_t	R	LWC
Convective	JS	2020	1.80	3.89	871	22.64	1.05
	Wen et al. (2017b)	2014−15	1.73	3.84	846	19.10	0.88
	FJ	2020	1.84	3.95	1047	24.53	1.29
	Hu et al. (2022b)	2019	1.74	4.07	–	23.38	1.21
Stratiform	JS	2020	1.06	3.69	200	1.72	0.11
	Wen et al. (2017b)	2014−15	1.19	3.67	271	2.16	0.13
	FJ	2020	1.00	3.86	269	1.51	0.12
	Hu et al. (2022b)	2019	1.24	3.97	–	2.20	0.15

thereby the concave downward shape, has been explained by Wen et al. (2017b) and is not discussed further. Overall, convective rain has a higher concentration in every size bin and a larger maximum diameter than stratiform rain. The stratiform spectra were narrower, with a maximum diameter of approximately 4.7 mm. The raindrop concentration and maximum diameter also increased with increasing R (Fig. 7b), regarding incremental rain rate classes from <5 mm h^{-1} to 5–10 mm h^{-1}, 10–30 mm h^{-1}, and >30 mm h^{-1}. Similar characteristics were also observed for the Z classes (Fig. 7c).

The differences in raindrop concentration between presummer and Mei-yu rainfall were compared in each size bin by subtracting $N(d)$ of JS from $N(d)$ of FJ (Figs. 7d–f). One can conclude that pre-summer rainfall contains more small drops peaking at ~0.5 mm and extends to 1–2 mm size bins with intense rainfall. Accordingly, the higher C_t (up to 683.89) due to the extra small drops in pre-summer rainfall should be responsible for the slightly higher values of some DSD parameters than mei-yu. The influencing magnitude decreased with an increase in the DSD moment. The lower-ordered parameters (such as N_t) have a more pronounced

impact than the higher-ordered ones (such as Z).

3.3. *Vertical structures*

Eight-year GPM-DPR observations were applied to confirm the near-homogeneous DSD characteristics on the ground as derived above and to further investigate the statistics associated with vertical structures of monsoon rainfall microphysics. The Z_e, D_m, and lgN_w contoured frequencies by altitude diagrams (CFADs) from during April-May-June in FJ and June-July-August in JS are presented in Fig. 8. Note that the contaminated near-surface-level data due to ground clutter (<1 km height) were eliminated from the discussion. Similarities in the statistical vertical structure and evolution of precipitation in these two regions/periods can also be found in the satellite observations, consistent with the rainfall microphysics similarities described in the previous paragraphs from ground-based Parsivel observations.

For convective rain of pre-summer rainfall in FJ and mei-yu rainfall in JS, the altitude of the majority (>30% of the maximum frequency) of 30-dBZ distributions for convective rain is near 6-km height, suggesting the general formation
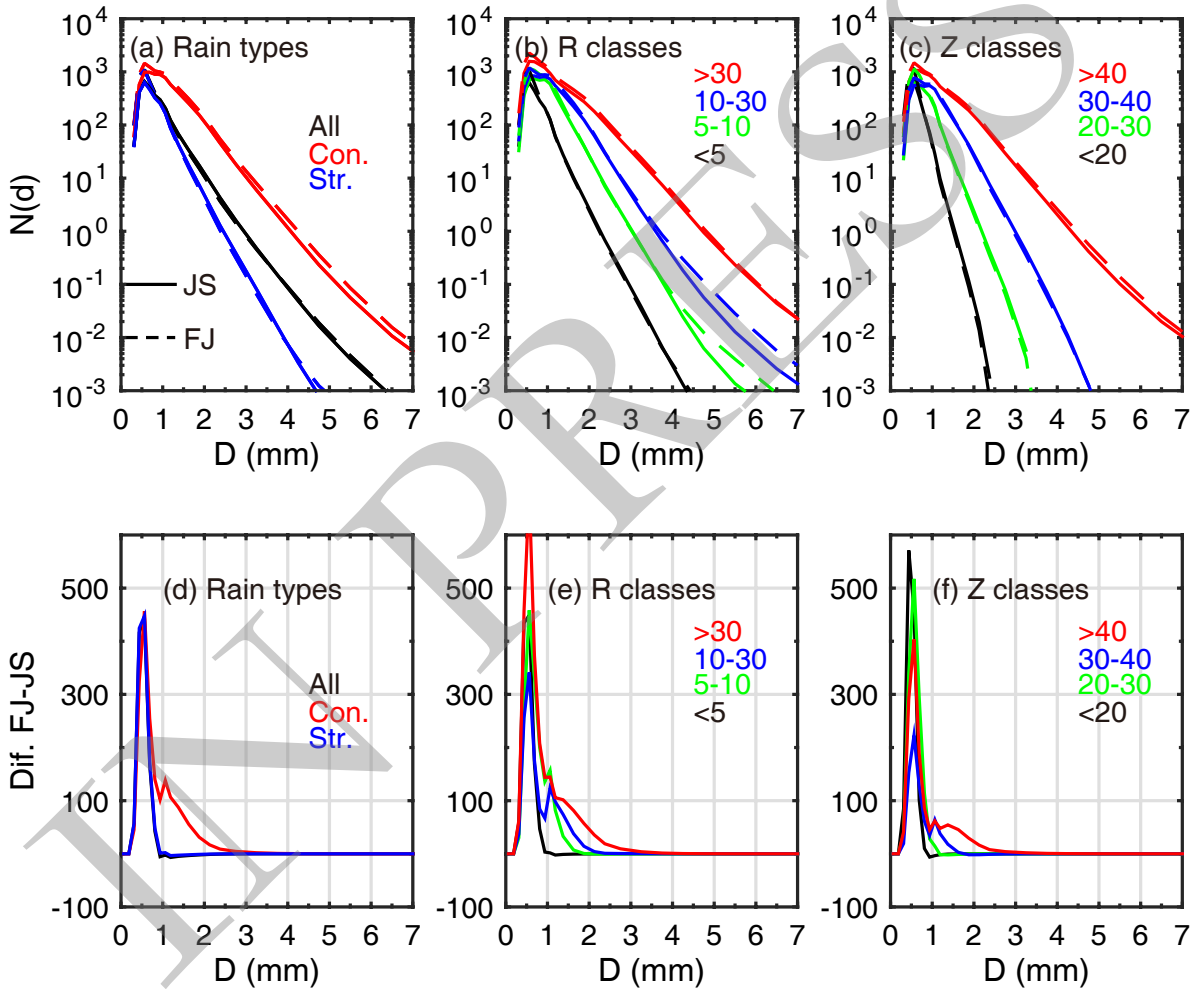
Fig. 7. Composite raindrop spectrum curves for different (a) rain types, (b) R classes, and (c) Z classes. The solid and dashed lines represent rainfall in JS and FJ, respectively. (d–f) Differences in $N(d)$ between FJ and JS with variable colors corresponding to different classes.
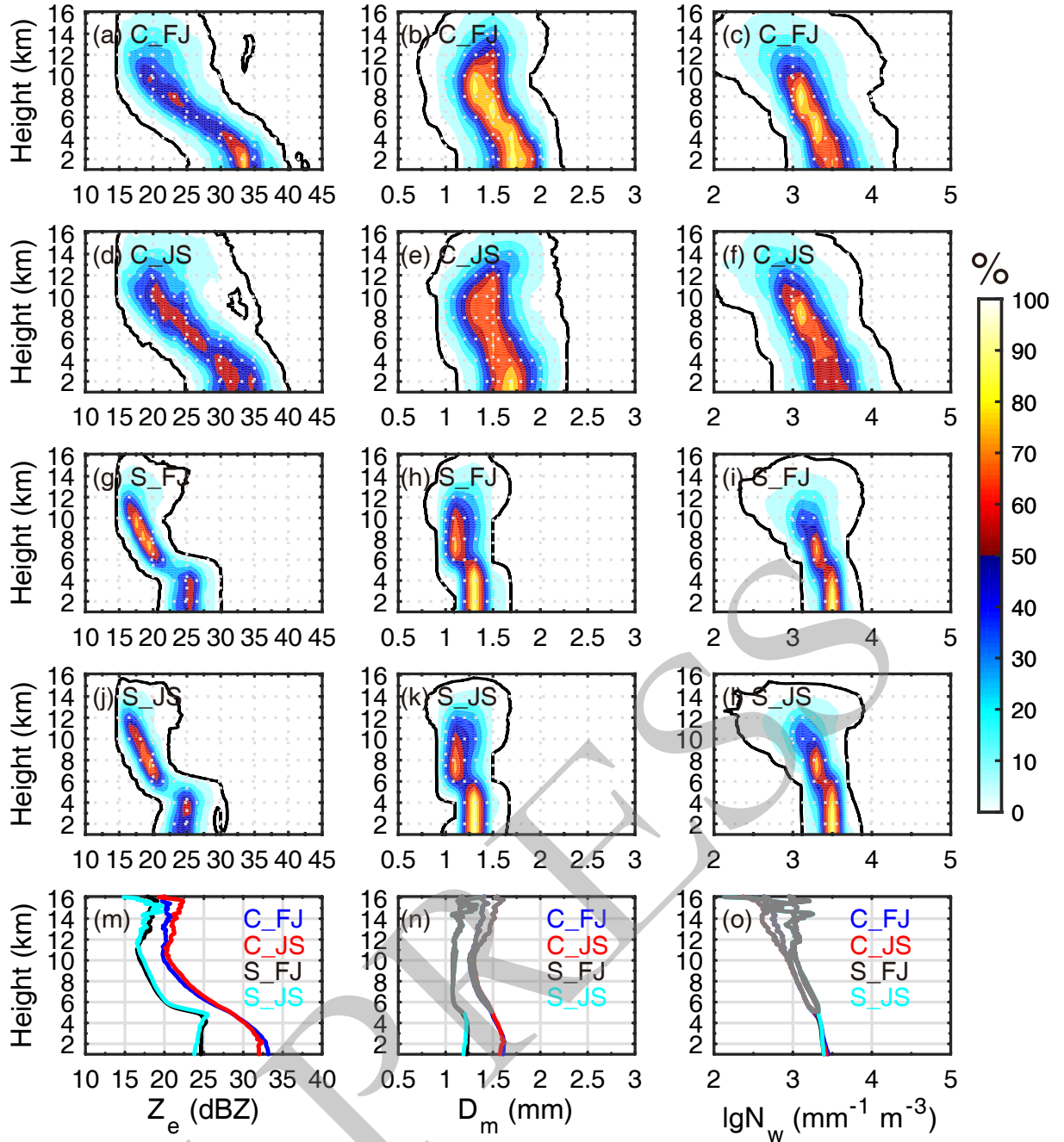
Fig. 8. Vertical profiles of (left) Z_e, (middle) D_m, and (right) $\lg N_w$ for convective (C_) and stratiform (S_) rain in FJ and JS. Shaded colors represent the frequency of occurrence relative to the maximum absolute frequency in the data sample represented in the CFAD. (m–o) The blue and red (black and cyan) lines represent the averaged convective (stratiform) rainfall values in FJ and JS, respectively.

of moderate convection within warm clouds (Chen et al., 2019; Wen et al., 2020). The sharp decrease in convective Z_e at altitudes above the freezing level indicates a limited amount of large frozen hydrometeors and super-cooled water (Carr et al., 2017; Wen et al., 2020). Consequently, large raindrops were rare near the ground. Below the 0°C isotherm level, the convective Z_e continued to increase until a height of 1 km, with the convective core centered at ~ 32–35 dBZ. The average convective Z_e in FJ was only

~1 dBZ higher than in JS.

The corresponding convective D_m and $\lg N_w$ CFADs exhibited negligible differences. Typically, below the 0°C isotherm level, the average profiles of convective D_m and $\lg N_w$ for FJ and JS were nearly identical (Figs. 8n, o). From a height of 4 km to ~2 km, the rapid increase in Z_e was associated with an increase in both D_m and $\lg N_w$, implying the combined effects of coalescence and warm rain accretion, noting that the warm rain microphysical processes related to DSD

include rain evaporation, accretion, and sedimentation (Carey and Rutledge, 2000; Zhang et al., 2008). While the coalescence process increased the raindrop size and decreased the concentration, the accretion process had the opposite effect. The evaporation distinctly decreases the concentration of raindrops but should be negligible under such a humid environment in the persistent EASM rainband (Wen et al., 2020). Meanwhile, the DSD often narrows because of size sorting by the differential sedimentation of falling particles (Milbrandt and Yau, 2005; Dawson et al., 2010). However, in a statistical sense, size sorting is transient and does not substantially impact the overall DSD characteristics (Bailey and Hallett, 2009), especially during moderate convection within the widespread stratiform area of quasi-stationary and continuous monsoonal rainfall (Kumjian and Ryzhkov, 2012; Wen et al., 2020). From a height of 2 km downward to 1 km, the convective D_m decreases slightly while the $\lg N_w$ value continues to increase. These characteristics may have been associated with an overpowered breakup rather than a coalescence process.

For stratiform rain, the CFADs and mean vertical profiles of the examined parameters show an even more homogeneous pattern for FJ and JS. The stratiform Z_e and D_m at all altitudes were lower than those of convective rain, with an enhanced reflectivity area (bright band, ~25.5 dBZ) around the 5-km height (near the 0°C isotherm level). The stratiform Z_e also decreases rapidly at an altitude above the 0°C isotherm level. In contrast, it shows only a weak decreasing trend (ranging between 20 dBZ and 30 dBZ) when descending toward the ground. The decrease in stratiform D_m and increase in $\lg N_w$ below the melting layer can be attributed to the breakup process (Rosenfeld and Ulbrich, 2003).

To investigate the potential anomalous characteristics that might be responsible for the heavy rainfall during 2020, the differences in the vertical profiles for convective and stratiform rain in FJ and JS between 2020 and the eight-year statistics were presented in Fig. 9. As shown, monsoon rainfall in 2020 exhibited minor anomalies in the vertical structure of its precipitation microphysics. Typically, convective rain in FJ was slightly weaker, with the maximum difference in Z_e being lower than 1 dBZ. In contrast, convective JS rainfall was stronger in 2020 than the eight-year average, but the differences are still lower than 1.5 dBZ (below 14 km height). The convective D_m showed a differential pattern similar to that of Z_e, whereas the $\lg N_w$ did the opposite. In other words, the heavy rainfall during 2020 in JS (FJ) was associated with a slightly stronger (lower) than average convection with a ~0.1 mm larger D_m (~0.1 mm^{-1} m^{-3} lower $\lg N_w$). The differences in stratiform Z_e were still lower than 1 dBZ for both JS and FJ, and they all contain a ~0.8 dBZ stronger bright band. The differences in stratiform D_m and $\lg N_w$ were even smaller. The comparison of the vertical structure of precipitation between 2020 and the eight-year average revealed a negligible difference in annual EASM rainfall microphysics.

Generally, the GPM-derived precipitation microphysics is a typical monsoon rainfall feature in East China, which is consistent with polarimetric radar observations (Shusse et al., 2009; Oue et al., 2011, 2015; Chang et al., 2015; Wen et al., 2020; Chen et al., 2022). Both Wen et al. (2020) and the current study target the vital role of warm rain processes during the evolution of the summer/mei-yu convective rainfall in this specific region. It is worth noting that the different working principles, data samples, and processing procedures can all contribute to the differences between the GPM and ground-based observations. Despite their slight differences, the high uniformity of the vertical distribution and pattern of precipitation microphysics between FJ and JS as derived from the GPM (for both summer 2020 and the eight-year average) is another indicator that supports the disdrometer-observed, near-homogeneous DSDs.

In summary, observations from the disdrometer, polarimetric radar, and satellite-borne radar in the present and previous studies cooperatively brought us to a consensus. There was inherent homogeneous precipitation microphysics (with slight regional deviations) during the northward migration of the quasi-stationary EASM front and the associated rainband in East China. With near-homogeneous precipitation microphysics, the long-lasting duration of rainfall, as opposed to differences in precipitation microphysics, was responsible for the record-breaking monsoonal rainfall in 2020 over this specific region.

4.   Conclusion and discussion

This study uses observations from 96 Parsivel disdrometers to reveal the microphysical characteristics of the record-breaking 2020 summer/mei-yu rainfall over East China. The associated vertical structure and evolution of precipitation during the northward migration of the EASM rainband, from the pre-summer season in Fujian to the mei-yu season in Jiangsu province, were further investigated using eight-year GPM-2ADPR data. The main conclusions are summarized as follows.

(1) Due to the earlier northward migration of the summer monsoon rainband from South/Southeast China to the Yangtze-Huaihe river valley of East China in 2020, JS experienced nearly twice as heavy rainfall than FJ, with mean daily rainfall amounts of 10.47 mm d^{-1} over JS and 5.41 mm d^{-1} over FJ. However, the near-equal contribution of convective rain between pre-summer rainfall in FJ and mei-yu rainfall in JS implicates rainfall duration (instead of intensity) in determining rainfall amounts in the two regions/periods.

(2) Considering the wide range of observational stations between FJ and JS, comprehensive comparisons of all DSD parameters and composite spectra between pre-summer and mei-yu rainfall were very similar, with negligible differences. The only noticeable difference is the higher numbers (nearly 500) of 0.5–1 mm size raindrops per minute with intense rainfall in FJ because of the higher moisture content in the ambient atmosphere of the coastal FJ. Generally, the
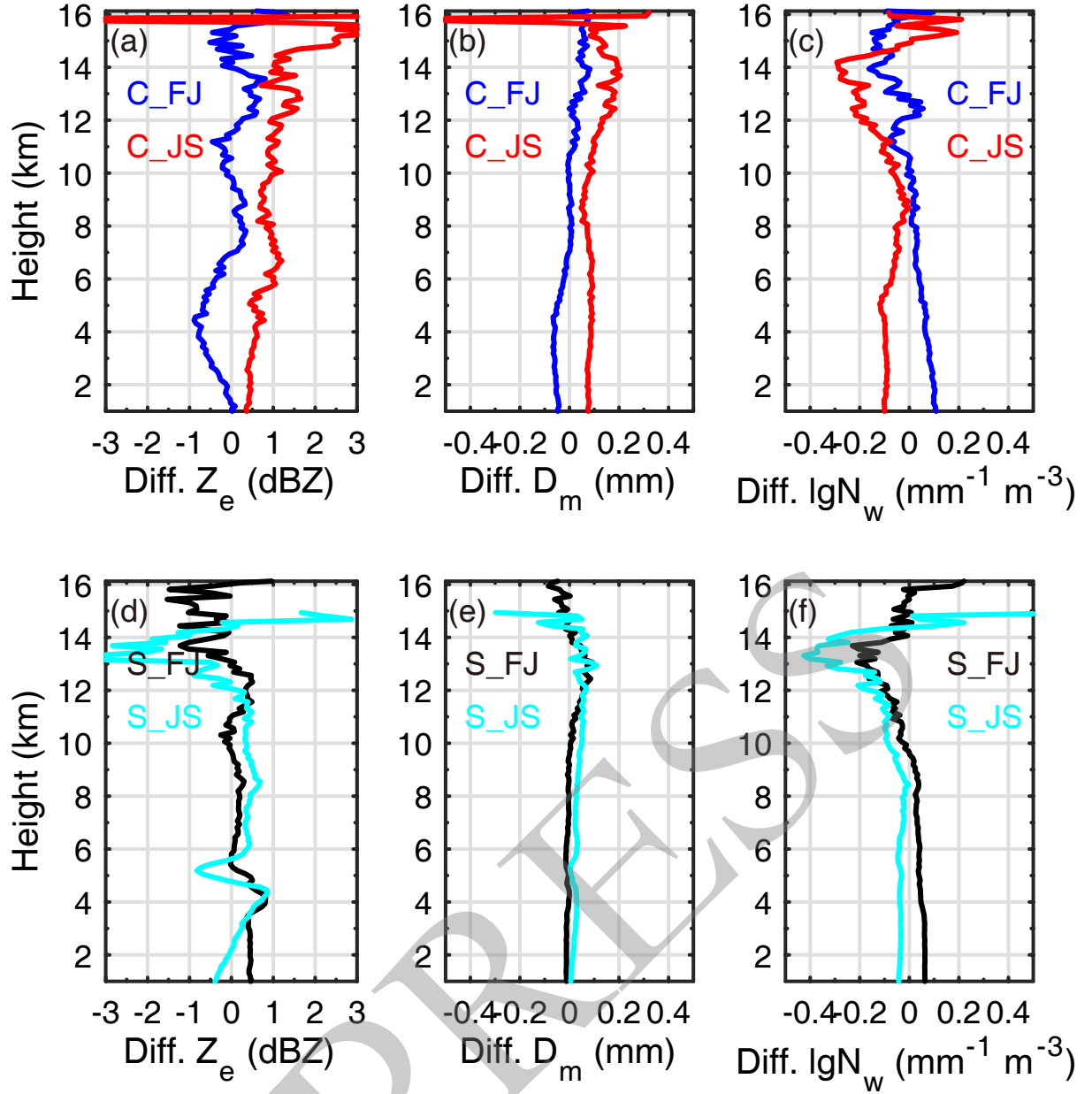
Fig. 9. Differences in the vertical profiles of averaged (left) Z_e, (middle) D_m, and (right) $\lg N_w$ for convective (C_) and stratiform (S_) rain in FJ and JS between 2020 and the eight-year statistics.

record-breaking 2020 summer monsoon rainfall should largely be attributed to the unusually long duration of mei-yu rainfall for this year, with inherent similarities in precipitation microphysics, typical of a near-maritime rainfall feature (high concentrations of small-sized raindrops), with only slight regional variations. This finding is consistent with previous results for the same or surrounding climatic regimes.

(3) The similarity in monsoon rainfall DSD is associated with a similar statistical vertical structure and evolution of microphysics in these two regions/periods. The Z_e, D_m, and $\lg N_w$ CFADs for both convective and stratiform rain exhibited typical monsoon rainfall features. The competition between different rain-forming processes during moderate convective rainfall resulted in this region's unique and near-homoge-

neous precipitation microphysics. Overall, observations from disdrometers and satellite-borne radar, as presented here, as well as many previous disdrometer and polarimetric radar analyses, jointly demonstrate the robust conclusion of inherent near-homogeneous precipitation microphysics during the northward migration of the quasi-stationary EASM rainband in East China. Ding et al. (2010) stated that the EASM is the dominant moisture supplier for persistent heavy rainfall in East China. Every summer, East China is controlled by a similar large-scale circulation able to transport abundant water vapor from the Bay of Bengal, the South China Sea, and/or the western Pacific Ocean by southerly winds. Consequently, the generation and evolution of precipitation may have exhibited similar characteristics. In a statisti-

cal sense, the consequent precipitation microphysics showed inherent homogeneous characteristics despite slight regional variations, at least over a wide range of East China. The conclusions we obtained reveal that the differences investigated in the literature are within one standard deviation of the general EASM rainfall microphysics. This study fills the gaps (differences) in the literature and will prove helpful for the future development of general and applicable microphysics parameterization for EASM rainfall in East China. In addition, the fitted D_m–lgN_w lines have potential application value for more accurate DSD retrieval from the GPM observations. In the interests of disaster prevention and mitigation, further efforts are needed to apply disdrometer-derived and GPM-retrieved information to conduct more accurate quantitative precipitation estimations and model simulations.

REFERENCES

Bailey, M. P., and J. Hallett, 2009: A comprehensive habit diagram for atmospheric ice crystals: Confirmation from the laboratory, AIRS II, and other field studies. *J. Atmos. Sci.*, **66**, 2888−2899, https://doi.org/10.1175/2009JAS2883.1.

Battaglia, A., E. Rustemeier, A. Tokay, U. Blahak, and C. Simmer, 2010: PARSIVEL snow observations: A critical assessment. *J. Atmos. Oceanic Technol.*, **27**, 333−344, https://doi.org/10.1175/2009JTECHA1332.1.

Bringi, V. N., V. Chandrasekar, J. Hubbert, E. Gorgucci, W. L. Randeu, and M. Schoenhuber, 2003: Raindrop size distribution in different climatic regimes from disdrometer and dual-polarized radar analysis. *J. Atmos. Sci.*, **60**, 354−365, https://doi.org/10.1175/1520-0469(2003)060<0354:RSDIDC>2.0.CO;2.

Bringi, V. N., M. Thurai, K. Nakagawa, G. J. Huang, T. Kobayashi, A. Adachi, H. Hanado, and S. Sekizawa, 2006: Rainfall estimation from C-band polarimetric radar in Okinawa, Japan: Comparisons with 2D-video disdrometer and 400MHz wind profiler. *J. Meteor. Soc. Japan*, **84**, 705−724,

https://doi.org/10.2151/jmsj.84.705.

Carey, L. D., and S. A. Rutledge, 2000: The relationship between precipitation and lightning in tropical island convection: A C-band polarimetric radar study. *Mon. Wea. Rev.*, **128**, 2687−2710, https://doi.org/10.1175/1520-0493(2000)128<2687:TRBPAL>2.0.CO;2.

Carr, N., P. E. Kirstetter, J. J. Gourley, and Y. Hong, 2017: Polarimetric signatures of midlatitude warm-rain precipitation events. *J. Appl. Meteorol. Climatol.*, **56**, 697−711, https://doi.org/10.1175/JAMC-D-16-0164.1.

Chang, W.-Y., W.-C. Lee, and Y.-C. Liou, 2015: The kinematic and microphysical characteristics and associated precipitation efficiency of subtropical convection during SoWMEX/TiMREX. *Mon. Wea. Rev.*, **143**, 317−340, https://doi.org/10.1175/MWR-D-14-00081.1.

Chang, Y., X. L. Guo, J. Tang, and G. X. Lu, 2019: Aircraft measurement campaign on summer cloud microphysical properties over the Tibetan Plateau. *Scientific Reports*, **9**, 4912, https://doi.org/10.1038/s41598-019-41514-5.

Chen, B. J., J. Yang, and J. P. Pu, 2013: Statistical characteristics of raindrop size distribution in the Meiyu season observed in Eastern China. *J. Meteor. Soc. Japan*, **91**, 215−227, https://doi.org/10.2151/jmsj.2013-208.

Chen, F. J., X. Y. Zheng, H. Y. Wen, and Y. Yuan, 2022: Microphysics of convective and stratiform precipitation during the summer monsoon season over the Yangtze–Huaihe River Valley, China. *Journal of Hydrometeorology*, **23**, 239−252, https://doi.org/10.1175/JHM-D-21-0078.1.

Chen, G., and Coauthors, 2019: Microphysical characteristics of three convective events with intense rainfall observed by polarimetric radar and disdrometer in Eastern China. *Remote Sensing*, **11**, 2004, https://doi.org/10.3390/rs11172004.

Chen, Y., 2009: The characteristic of drop size distribution during SoWMEX. M.S. thesis, Institute of Atmospheric Physics, NCU, Chungli, Taiwan, 68 pp. (in Chinese)

Clark, R. T., X. Q. Dong, C.-H. Ho, J. H. Sun, H. L. Yuan, and T. Takemi, 2021: Preface to the special issue on summer 2020: Record rainfall in Asia—Mechanisms, predictability and impacts. *Adv. Atmos. Sci.*, **38**, 1977−1979, https://doi.org/10.1007/s00376-021-1010-5.

Dawson, D. T., M. Xue, J. A. Milbrandt, and M. K. Yau, 2010: Comparison of evaporation and cold pool development between single-moment and multimoment bulk microphysics schemes in idealized simulations of tornadic thunderstorms. *Mon. Wea. Rev.*, **138**, 1152−1171, https://doi.org/10.1175/2009MWR2956.1.

Ding, Y. H., and J. C. L. Chan, 2005: The East Asian summer monsoon: An overview. *Meteorol. Atmos. Phys.*, **89**, 117−142, https://doi.org/10.1007/s00703-005-0125-z.

Ding, Y. H., Y. J. Liu, Y. Sun, and Y. F. Song, 2010: Weakening of the Asian summer monsoon and its impact on the precipitation pattern in China. *International Journal of Water Resources Development*, **26**, 423−439, https://doi.org/10.1080/07900627.2010.492607.

Ding, Y. H., Y. Y. Liu, and Z.-Z. Hu, 2021: The record-breaking Mei-yu in 2020 and associated atmospheric circulation and tropical SST anomalies. *Adv. Atmos. Sci.*, **38**, 1980−1993, https://doi.org/10.1007/s00376-021-0361-2.

Fu, Z. K., X. Q. Dong, L. L. Zhou, W. J. Cui, J. Y. Wang, R. Wan, L. Leng, and B. K. Xi, 2020: Statistical characteristics of raindrop size distributions and parameters in Central China during the Meiyu seasons. *J. Geophys. Res.: Atmos.*,

125, e2019JD031954, https://doi.org/10.1029/2019JD03 1954.

Hersbach, H., and Coauthors, 2020: The ERA5 global reanalysis. *Quart. J. Roy. Meteor. Soc.*, **146**, 1999−2049, https://doi.org/10.1002/qj.3803.

Hu, X., W. H. Ai, J. Q. Qiao, S. S. Hu, D. Han, and W. Yan, 2022a: Microphysics of Summer Precipitation Over Yangtze-Huai River Valley region in China Revealed by GPM DPR Observation. *Earth and Space Science*, **9**, e2021EA002021, https://doi.org/10.1029/2021EA002021.

Hu, Y. J., W. Zhang, Y. X. Zhang, and L. Wen, 2022b: Comparative analysis of raindrop size distribution characteristics before and after monsoon onset in southern coast of Fujian province in 2018−2019. *Acta Meteorologica Sinica*, **80**, 618−631, https://doi.org/10.11676/qxxb2022.045. (in Chinese with English abstract)

Huang, H., K. Zhao, P. L. Fu, H. N. Chen, G. Chen, and Y. Zhang, 2021: Validation of precipitation measurements from the dual-frequency precipitation radar onboard the GPM core observatory using a polarimetric radar in South China. *IEEE Trans. Geosci. Remote Sens.*, **60**, 4104216, https://doi.org/10.1109/TGRS.2021.3118601.

Huo, Z. Y., Z. Ruan, M. Wei, R. S. Ge, F. Li, and Y. Ruan, 2019: Statistical characteristics of raindrop size distribution in South China summer based on the vertical structure derived from VPR-CFMCW. *Atmospheric Research*, **222**, 47−61, https://doi.org/10.1016/j.atmosres.2019.01.022.

Iguchi, T., and Coauthors, 2021: GPM/DPR level-2 algorithm theoretical basis document. NASA Goddard Space Flight Center.

Jin, Q., Y. Yuan, H. J. Liu, C. E. Shi, and J. B. Li, 2015: Analysis of microphysical characteristics of the raindrop spectrum over the area between the Yangtze River and the Huaihe River during summer. *Acta Meteorologica Sinica*, **73**, 778−788, https://doi.org/10.11676/qxxb2015.036. (in Chinese with English abstract)

Kumjian, M. R., and A. V. Ryzhkov, 2012: The impact of size sorting on the polarimetric radar variables. *J. Atmos. Sci.*, **69**, 2042−2060, https://doi.org/10.1175/JAS-D-11-0125.1.

Lai, R. Z., X. T. Liu, S. Hu, H. Xiao, F. Xia, L. Feng, and H. Q. Li, 2022: Raindrop size distribution characteristic differences during the dry and wet seasons in South China. *Atmospheric Research*, **266**, 105947, https://doi.org/10.1016/j.atmosres.2021.105947.

Lane, J., T. Kasparis, S. Michaelides, and P. Metzger, 2018: A phenomenological relationship between vertical air motion and disdrometer derived *A-b* coefficients. *Atmospheric Research*, **208**, 94−105, https://doi.org/10.1016/j.atmosres.2017.07.011.

Li, J. Y., and J. Y. Mao, 2019: Factors controlling the interannual variation of 30–60-day boreal summer intraseasonal oscillation over the Asian summer monsoon region. *Climate Dyn.*, **52**, 1651−1672, https://doi.org/10.1007/s00382-018-4216-1.

Li, L., C. W. Zhu, R. H. Zhang, and B. Q. Liu, 2021: Roles of the Tibetan Plateau vortices in the record Meiyu rainfall in 2020. *Atmospheric Science Letters*, **22**, e1017, https://doi.org/10.1002/asl.1017.

Liu, B. Q., Y. H. Yan, C. W. Zhu, S. M. Ma, and J. Y. Li, 2020: Record-breaking Meiyu rainfall around the Yangtze River in 2020 regulated by the subseasonal phase transition of the North Atlantic Oscillation. *Geophys. Res. Lett.*, **47**, e2020GL090342, https://doi.org/10.1029/2020GL090342.

Milbrandt, J. A., and M. K. Yau, 2005: A multimoment bulk micro-

physics parameterization. Part II: A proposed three-moment closure and scheme description. *J. Atmos. Sci.*, **62**, 3065−3081, https://doi.org/10.1175/JAS3535.1.

Murali Krishna, U. V., S. K. Das, E. G. Sulochana, U. Bhowmik, S. M. Deshpande, and G. Pandithurai, 2021: Statistical characteristics of raindrop size distribution over the Western Ghats of India: Wet versus dry spells of the Indian summer monsoon. *Atmospheric Chemistry and Physics*, **21**, 4741−4757, https://doi.org/10.5194/acp-21-4741-2021.

Niu, R. Y., P. M. Zhai, and G. R. Tan, 2021: Anomalous features of extreme Meiyu in 2020 over the Yangtze-Huai River basin and attribution to large-scale circulations. *J. Meteor. Res.*, **35**, 799−814, https://doi.org/10.1007/s13351-021-1018-x.

Oue, M., H. Uyeda, and D. I. Lee, 2011: Raindrop size distribution parameters estimated from polarimetric radar variables in convective cells around Okinawa Island during the Baiu period. *Asia-Pacific Journal of Atmospheric Sciences*, **47**, 33−44, https://doi.org/10.1007/s13143-011-1003-x.

Oue, M., T. Ohigashi, K. Tsuboki, and E. Nakakita, 2015: Vertical distribution of precipitation particles in Baiu frontal stratiform intense rainfall around Okinawa Island, Japan. *J. Geophys. Res.: Atmos.*, **120**, 5622−5637, https://doi.org/10.1002/2014JD022712.

Peng, S., 2020: 1-km monthly precipitation dataset for China (1901−2020). A Big Earth Data Platform for Three Poles, https://doi.org/10.5281/zenodo.3185722. [Available online from http://www.tpdc.ac.cn/zh-hans/data/faae7605-a0f2-4d18-b28f-5cee413766a2/]

Qiao, S. B., and Coauthors, 2021: The longest 2020 Meiyu season over the past 60 years: Subseasonal perspective and its predictions. *Geophys. Res. Lett.*, **48**, e2021GL093596, https://doi.org/10.1029/2021GL093596.

Raut, B. A., and Coauthors, 2021: Microphysical origin of raindrop size distributions during the Indian monsoon. *Geophys. Res. Lett.*, **48**, e2021GL093581, https://doi.org/10.1029/2021GL093581.

Rosenfeld, D., and C. W. Ulbrich, 2003: Cloud microphysical properties, processes, and rainfall estimation opportunities. *Meteor. Monogr.*, **30**, 237−258, https://doi.org/10.1175/0065-9401(2003)030<0237:CMPPAR>2.0.CO;2.

Ryu, J., H. J. Song, B. J. Sohn, and C. Liu, 2021: Global distribution of three types of drop size distribution representing heavy rainfall from GPM/DPR measurements. *Geophys. Res. Lett.*, **48**, e2020GL090871, https://doi.org/10.1029/2020GL090871.

Seela, B. K., J. Janapati, P. L. Lin, K. K. Reddy, R. Shirooka, and P. K. Wang, 2017: A comparison study of summer season raindrop size distribution between Palau and Taiwan, two Islands in Western Pacific. *J. Geophys. Res.: Atmos.*, **122**, 11 787−11 805, https://doi.org/10.1002/2017JD026816.

Seto, S., T. Iguchi, R. Meneghini, J. Awaka, T. Kubota, T. Masaki, and N. Takahashi, 2021: The precipitation rate retrieval algorithms for the GPM Dual-frequency Precipitation Radar. *J. Meteor. Soc. Japan*, **99**, 205−237, https://doi.org/10.2151/jmsj.2021-011.

Shusse, Y., K. Nakagawa, N. Takahashi, S. Satoh, and T. Iguchi, 2009: Characteristics of polarimetric radar variables in three types of rainfalls in a Baiu front event over the East China Sea. *J. Meteor. Soc. Japan*, **87**, 865−875, https://doi.org/10.2151/jmsj.87.865.

Sun, Y. T., X. Q. Dong, W. J. Cui, Z. M. Zhou, Z. K. Fu, L. L. Zhou, Y. Deng, and C. G. Cui, 2020: Vertical structures of

typical meiyu precipitation events retrieved from GPM-DPR. *J. Geophys. Res.: Atmos.*, **125**, e2019JD031466, https://doi.org/10.1029/2019JD031466.

Takaya, Y., I. Ishikawa, C. Kobayashi, H. Endo, and T. Ose, 2020: Enhanced Meiyu-Baiu rainfall in early summer 2020: Aftermath of the 2019 super IOD event. *Geophys. Res. Lett.*, **47**, e2020GL090671, https://doi.org/10.1029/2020GL090671.

Tang, Q., H. Xiao, C. W. Guo, and L. Feng, 2014: Characteristics of the raindrop size distributions and their retrieved polarimetric radar parameters in northern and southern China. *Atmospheric Research*, **135–136**, 59–75, https://doi.org/10.1016/j.atmosres.2013.08.003. https://doi.org/10.1016/j.atmosres.2013.08.003.

Tao, S.-Y., and L.-X. Chen, 1987: A review of recent research on the East Asian summer monsoon in China. *Monsoon Meteorology*, C.-P. Chang and T. N. Krishnamurti, Eds., Oxford Universtiy Press, 60–92.

Thurai, M., V. N. Bringi, and P. T. May, 2010: CPOL radar-derived drop size distribution statistics of stratiform and convective rain for two regimes in Darwin, Australia. *J. Atmos. Oceanic Technol.*, **27**, 932–942, https://doi.org/10.1175/2010JTECHA1349.1.

Tokay, A., and D. A. Short, 1996: Evidence from tropical raindrop spectra of the origin of rain from stratiform versus convective clouds. *J. Appl. Meteorol.*, **35**, 355–371, https://doi.org/10.1175/1520-0450(1996)035<0355:EFTRSO>2.0.CO;2.

Tokay, A., W. A. Petersen, P. Gatlin, and M. Wingo, 2013: Comparison of raindrop size distribution measurements by collocated disdrometers. *J. Atmos. Oceanic Technol.*, **30**, 1672–1690, https://doi.org/10.1175/JTECH-D-12-00163.1.

Tokay, A., D. B. Wolff, and W. A. Petersen, 2014: Evaluation of the new version of the laser-optical disdrometer, OTT Parsivel 2. *J. Atmos. Oceanic Technol.*, **31**, 1276–1288, https://doi.org/10.1175/JTECH-D-13-00174.1.

Uijlenhoet, R., M. Steiner, and J. A. Smith, 2003: Variability of raindrop size distributions in a squall line and implications for radar rainfall estimation. *Journal of Hydrometeorology*, **4**, 43–61, https://doi.org/10.1175/1525-7541(2003)004<0043:VORSDI>2.0.CO;2.

Vivekanandan, J., G. F. Zhang, and E. Brandes, 2004: Polarimetric radar estimators based on a constrained gamma drop size distribution model. *J. Appl. Meteorol.*, **43**, 217–230, https://doi.org/10.1175/1520-0450(2004)043<0217:PREBOA>2.0.CO;2.

Wang, G. L., R. Li, J. S. Sun, X. D. Xu, R. R. Zhou, and L. P. Liu, 2022: Comparative analysis of the characteristics of rainy season raindrop size distributions in two typical regions of the Tibetan Plateau. *Adv. Atmos. Sci.*, **39**, 1062–1078, https://doi.org/10.1007/s00376-021-1135-6.

Wang, J., Y. J. Liu, Y. H. Ding, and Z. L. Wu, 2021a: Towards influence of Arabian Sea SST anomalies on the withdrawal date of Meiyu over the Yangtze-Huaihe River basin. *Atmospheric Research*, **249**, 105340, https://doi.org/10.1016/j.atmosres.2020.105340.

Wang, L. C., X. G. Sun, X. Q. Yang, L. F. Tao, and Z. Q. Zhang, 2021b: Contribution of water vapor to the record-breaking extreme Meiyu rainfall along the Yangtze River valley in 2020. *J. Meteor. Res.*, **35**, 557–570, https://doi.org/10.1007/s13351-021-1030-1.

Wen, L., K. Zhao, G. F. Zhang, M. Xue, B. W. Zhou, S. Liu, and X. C. Chen, 2016: Statistical characteristics of raindrop size distributions observed in East China during the Asian Summer Monsoon Season using 2-D video disdrometer and micro rain radar data. *J. Geophys. Res.: Atmos.*, **121**, 2265–2282, https://doi.org/10.1002/2015JD024160.

Wen, J., and Coauthors, 2017a: Evolution of microphysical structure of a subtropical squall line observed by a polarimetric radar and a disdrometer during OPACC in Eastern China. *J. Geophys. Res.: Atmos.*, **122**, 8033–8050, https://doi.org/10.1002/2016JD026346.

Wen, L., K. Zhao, G. F. Zhang, S. Liu, and G. Chen, 2017b: Impacts of instrument limitations on estimated raindrop size distribution, radar parameters, and model microphysics during Mei-Yu season in East China. *J. Atmos. Oceanic Technol.*, **34**, 1021–1037, https://doi.org/10.1175/JTECH-D-16-0225.1.

Wen, L., and Coauthors, 2018: Drop size distribution characteristics of seven typhoons in China. *J. Geophys. Res.: Atmos.*, **123**, 6529–6548, https://doi.org/10.1029/2017JD027950.

Wen, L., K. Zhao, M. Y. Wang, and G. F. Zhang, 2019: Seasonal variations of observed raindrop size distribution in East China. *Adv. Atmos. Sci.*, **36**, 346–362, https://doi.org/10.1007/s00376-018-8107-5.

Wen, L., K. Zhao, Z. L. Yang, H. N. Chen, H. Huang, G. Chen, and Z. W. Yang, 2020: Microphysics of stratiform and convective precipitation during Meiyu season in Eastern China. *J. Geophys. Res.: Atmos.*, **125**, e2020JD032677, https://doi.org/10.1029/2020JD032677.

Zhang, A. S., and Coauthors, 2019a: Statistical characteristics of raindrop size distribution in the monsoon season observed in Southern China. *Remote Sensing*, **11**, 432, https://doi.org/10.3390/rs11040432.

Zhang, G., J. Vivekanandan, and E. Brandes, 2001: A method for estimating rain rate and drop size distribution from polarimetric radar measurements. *IEEE Trans. Geosci. Remote Sens.*, **39**, 830–841, https://doi.org/10.1109/36.917906.

Zhang, G. F., M. Xue, Q. Cao, and D. Dawson, 2008: Diagnosing the intercept parameter for exponential raindrop size distribution based on video disdrometer observations: Model development. *J. Appl. Meteorol. Climatol.*, **47**, 2983–2992, https://doi.org/10.1175/2008JAMC1876.1.

Zhang, G. F., and Coauthors, 2019b: Current status and future challenges of weather radar polarimetry: Bridging the gap between radar meteorology/hydrology/engineering and numerical weather prediction. *Adv. Atmos. Sci.*, **36**, 571–588, https://doi.org/10.1007/s00376-019-8172-4.

Zhang, W. J., Z. C. Huang, F. Jiang, M. F. Stuecker, G. S. Chen, and F. F. Jin, 2021: Exceptionally persistent Madden-Julian Oscillation activity contributes to the extreme 2020 East Asian summer monsoon rainfall. *Geophys. Res. Lett.*, **48**, e2020GL091588, https://doi.org/10.1029/2020GL091588.

Zheng, H. P., Y. Zhang, L. F. Zhang, H. C. Lei, and Z. H. Wu, 2021: Precipitation microphysical processes in the inner rainband of tropical cyclone Kajiki (2019) over the South China Sea revealed by polarimetric radar. *Adv. Atmos. Sci.*, **38**, 65–80, https://doi.org/10.1007/s00376-020-0179-3.

Zhou, Z.-Q., S.-P. Xie, and R. H. Zhang, 2021: Historic Yangtze flooding of 2020 tied to extreme Indian Ocean conditions. *Proceedings of the National Academy of Sciences of the United States of America*, **118**, e2022255118, https://doi.org/10.1073/pnas.2022255118.